

Article

Performance Analysis of Direct GPS Spoofing Detection Method with AHRS/Accelerometer

Keum-Cheol Kwon and Duk-Sun Shim *

School of Electrical and Electronics Engineering, Chung-Ang University, 84 Huksuk-ro, Dongjak-ku, Seoul 06974, Korea; kckwon@cau.ac.kr

* Correspondence: dshim@cau.ac.kr; Tel.: +82-2-820-5329

Received: 6 January 2020; Accepted: 1 February 2020; Published: 11 February 2020



Abstract: The global positioning system (GPS) is an essential technology that provides positioning capabilities and is used in various applications such as navigation, surveying, mapping, robot simultaneous localization and mapping (SLAM), location-based service (LBS), etc. However, the GPS is known to be vulnerable to intentional attacks such as spoofing because of its simple signal structure. In this study, a direct method is proposed for GPS spoofing detection, using Attitude and Heading Reference System (AHRS) accelerometer and analyzing the detection performance with corresponding probability density functions (PDFs). The difference in the acceleration between the GPS receiver and the accelerometer is used to detect spoofing. The magnitude of the acceleration error may be used as a decision variable. Additionally, using the magnitude of the north (or east) component of the acceleration error as another decision variable is proposed, which shows better performance in some conditions. The performance of the two decision variables is compared by calculating the probability of spoofing detection and the detectable minimum spoofing acceleration (DMSA), given a pre-defined false alarm probability and a pre-defined detection probability. It turns out that both decision variables need to be used together to obtain the best spoofing detection performance.

Keywords: GPS; spoofing detection; AHRS; accelerometer; Shim probability density function

1. Introduction

The global navigation satellite system (GNSS) is an essential technology for positioning and timing, and its application covers various areas such as navigation, surveying, mapping, robot simultaneous localization and mapping (SLAM), location-based service (LBS), etc. The global positioning system (GPS) is the original GNSS and its full operational capability (FOC) was declared in 1995 in the United States of America. The legacy L1 C/A code signal of GPS is very weak at the Earth's surface and has a simple structure to implement [1,2]. Thus, the GPS signal is vulnerable to intentional interferences such as jamming and spoofing. While jamming attacks make the GPS receivers malfunction, spoofing attacks make the target receiver unaware of it being attacked by thespoof. Spoofing threats have garnered attention since the initial finding of the 2001 Volpe Report [3]. GPS spoofers may cause significant damage to the target receiver by transmitting counterfeit navigation data which can result in erroneous navigation. Thus, spoofing attacks are a significant problem to users and many studies on spoofing attacks and anti-spoofing methods have been carried out since 2001.

Experiments have been conducted to understand the vulnerability of the GPS to spoofing [4,5], which proved that the GPS is not secure from spoofing. Some experiments tried to implement the spoofing itself [5–7]. A variety of approaches have been studied about spoofing detection of the GNSS [7–18] such as using received signal strength [9], signal quality monitoring at code and carrier levels [7], phase-only analysis of variance (ANOVA) method with generalized likelihood ratio test (GLRT) by employing dual antenna system [10], and using maximum likelihood estimator

(MLE) [11]. Prior studies [7,12] summarize various spoofing detection techniques, among which low complexity spoofing detection techniques include C/N_0 monitoring, absolute power monitoring, power variation versus receiver movement, code and phase rate consistency check, and GPS clock consistency check, while high complexity spoofing detection techniques include Direction Of Arrival (DOA) comparison [14] and consistency check with other solutions [15–18].

Among the effective high complexity spoofing detection techniques mentioned in the prior study [12], the DOA comparison approach uses the DOA measurements to assess the direction of the spoofing source and mitigates the interference by placing the spatial null in the antenna reception pattern [14]. The consistency check approach uses the inertial measurement unit (IMU) [15–18]. The relative platform trajectory estimated by the GNSS receiver is compared to the relative trajectory developed from the IMU measurement, specifically gyro output, to detect spoofing [15]. In References [16,17], a tightly coupled GPS / inertial navigation system (INS) is used to detect spoofing by incorporating fault detection concepts and Kalman filter, respectively, based on receiver autonomous integrity monitoring (RAIM). In [18], an accelerometer is used to detect spoofing by comparison of acceleration between the GPS receiver and the IMU. However, no prior research has been done on using the IMU and the acceleration error which is expressed with exact probability density function.

In this study, a direct GPS spoofing detection method is proposed which uses attitude and heading reference system (AHRS) and accelerometers via direct comparison of the acceleration estimated from the GPS receiver and the acceleration measured from IMU, which provides the acceleration error. The acceleration from the GPS receiver is estimated from the Kalman filter by including the acceleration as a state variable of the GPS dynamic system in this study, while the acceleration from the GPS receiver in Reference [18] is obtained from the difference of velocities which are estimated from the GPS Kalman filter. Two decision variables for spoofing detection are defined: the acceleration error from the acceleration of the GPS receiver and the acceleration from the AHRS/Accelerometer, expressed in the navigation frame. One decision variable is defined as the magnitude of the acceleration error, where only horizontal component is used, and the probability density function (PDF) of the decision variable is derived. It is called Shim PDF. The other decision variable is the magnitude of the north (or east) component of the acceleration error. The PDF of this decision variable is the folded Gaussian PDF. It was found that in the special condition that both moving acceleration and spoofing acceleration head around north (or east) together, the second decision variable of the magnitude of the north (or east) component provides better detection performance than the first decision variable of the magnitude of the horizontal component. Thus the magnitude of the horizontal acceleration error, the magnitude of the north component of the acceleration error, and the magnitude of the east component of the acceleration error are proposed to be used together to check whether one of these is greater than or equal to the corresponding threshold to detect the GPS spoofing.

Two performance measures are considered for spoofing detection. One is the probability of spoofing detection. The exact PDF for both decision variables is known and thus, for a given probability of false alarm, the detection threshold and the detection probability can be calculated. The other is the detectable minimum spoofing acceleration (DMSA), which is the magnitude of the minimum spoofing acceleration to obtain a pre-defined detection probability, given a pre-defined false alarm probability. The performances of the two decision variables for the two performance measures are compared and analyzed.

The structure of the first-half of the proposed direct GPS spoofing detection method is given in Section 2, which provides the acceleration error with GPS Kalman filter and AHRS. Section 3 defines the acceleration error, and two decision variables with their probability density functions, and shows the second-half of the proposed direct GPS spoofing detection method. The performance analysis of the proposed direct GPS spoofing detection method is given for two decision variables in Sections 4 and 5 using the two performance measures, the probability of detection and the DMSA. The conclusion is presented in Section 6.

2. The Structure of the First-half of the Proposed Direct GPS Spoofing Detection Method

2.1. Block Diagram to Obtain the Acceleration Error from GPS Receiver and Accelerometer

In this study, GPS spoofing detection is done by using the comparison of accelerations obtained from the GPS receiver and accelerometers. The block diagram of Figure 1 shows the procedure to obtain the difference of the two acceleration measurements. The accelerometers measure the specific force \hat{f}_{acc}^b and then, it is changed into \hat{f}_{acc}^n through the transformation matrix C_b^n . In \hat{f}_{acc}^b and \hat{f}_{acc}^n , the superscript b denotes the body frame and n denotes the navigation frame. The navigation frame uses the north(x)-east(y)-down(z) (NED) frame in this study. AHRS produces the transformation matrix C_b^n by using the sensor outputs and Kalman filter. C_b^n denotes the direction cosine matrix from the body frame to the navigation frame. The hat ($\hat{\cdot}$) denotes measured or calculated values containing errors and Ψ denotes the skew symmetric matrix of the attitude error.

It is assumed that IMU calibration and initial alignment is performed in advance depending on the characteristics of various inertial sensors since there are many kinds of gyroscopes, such as ring laser gyro, fiber optic gyro, hemispherical resonator gyro, and low cost micro-electro-mechanical system (MEMS) gyro, and so on, and different gyroscope has different error sources, and accelerometer has also many types, such as pendulous type, vibrating type, silicon type, and MEMS type. Figure 1 shows the IMU calibration and initial alignment with the dotted block, which will not be considered in this paper. Thus misalignment, bias, scale factor, and others are assumed to be compensated in advance. The IMU calibration and initial alignment is an essential process in the inertial navigation system and thus there are much research results which have been already performed [19,20]. Only GPS spoofing detection will be considered in this paper.

Matrices use capital letters, and vectors, small letters. Matrices and vectors will use bold letters and scalars use plain letters.

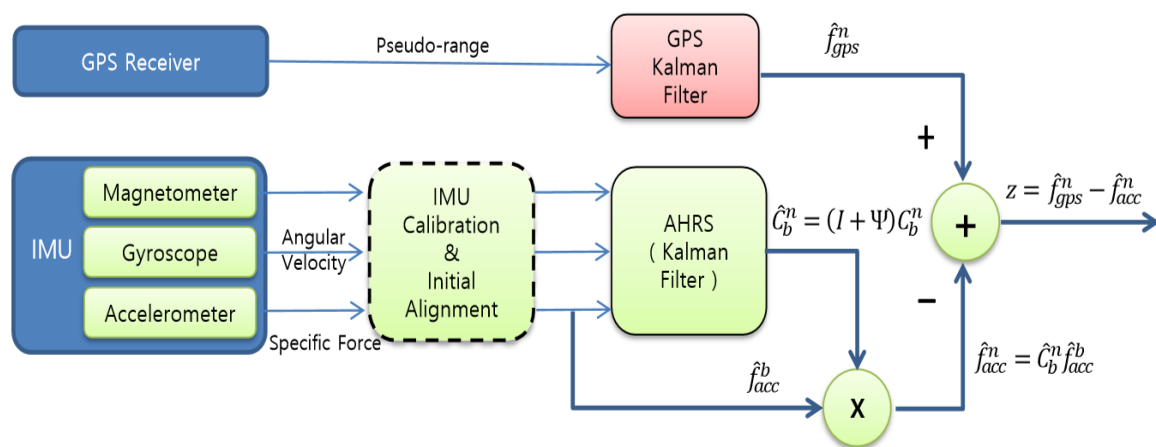


Figure 1. Block diagram to obtain the acceleration error from the Global Positioning System (GPS) receiver and accelerometer.

2.2. GPS Kalman Filter

The GPS receiver usually provides position and velocity information. To obtain acceleration from the GPS receiver, the Kalman filter is used by including acceleration as a state variable. The dynamics of the GPS receiver can be described by the state-space model as in Equation (1), which has 11 state variables such as 3-dimensional position, velocity, acceleration, GPS receiver's clock bias c_b , and drift c_d .

$$\dot{x}_{gps} = F_{gps}x_{gps} + w_{gps}. \quad (1)$$

where $x_{gps} = [x, \dot{x}, \ddot{x}, y, \dot{y}, \ddot{y}, z, \dot{z}, \ddot{z}, c_b, c_d]'$ and the state variable x_{gps} denotes the error state,

$$F_{gps} = \begin{bmatrix} F_X & O_{3 \times 3} & O_{3 \times 3} & O_{3 \times 3} \\ O_{3 \times 3} & F_Y & O_{3 \times 3} & O_{3 \times 3} \\ O_{3 \times 3} & O_{3 \times 3} & F_Z & O_{3 \times 3} \\ O_{2 \times 2} & O_{2 \times 2} & O_{2 \times 2} & F_W \end{bmatrix}, w_{gps} = \begin{bmatrix} w_X \\ w_Y \\ w_Z \\ w_W \end{bmatrix}, F_X = F_Y = F_Z = \begin{bmatrix} 0 & 1 & 0 \\ 0 & 0 & 1 \\ 0 & 0 & 0 \end{bmatrix}, F_W = \begin{bmatrix} 0 & 1 \\ 0 & 0 \end{bmatrix},$$

$$w_X = \begin{bmatrix} 0 \\ 0 \\ w_x \end{bmatrix}, w_Y = \begin{bmatrix} 0 \\ 0 \\ w_y \end{bmatrix}, w_Z = \begin{bmatrix} 0 \\ 0 \\ w_z \end{bmatrix}, w_W = \begin{bmatrix} w_b \\ w_d \end{bmatrix},$$

and w_x, w_y, w_z, w_b, w_d are independent white noises.

Pseudo range is the distance between the GPS satellite and the receiver. The difference between the measured pseudo range ρ_i and the estimated pseudo range $\hat{\rho}_i$ is used as the measurement in the Kalman filter for i-th GPS satellite

$$z_i = \hat{\rho}_i - \rho_i = H_i x_{gps} + v_i$$

where $H_i = [a_{xi} \ 0 \ 0 \ a_{yi} \ 0 \ 0 \ a_{zi} \ 0 \ 0 \ 1 \ 0]$, $a_{xi} = \frac{x_i - \hat{x}_u}{\hat{r}_i}$, $a_{yi} = \frac{y_i - \hat{y}_u}{\hat{r}_i}$, $a_{zi} = \frac{z_i - \hat{z}_u}{\hat{r}_i}$, $\hat{r}_i = \sqrt{(x_i - \hat{x}_u)^2 + (y_i - \hat{y}_u)^2 + (z_i - \hat{z}_u)^2}$, (x_i, y_i, z_i) is the position of i-th GPS satellite, $(\hat{x}_u, \hat{y}_u, \hat{z}_u)$ is the estimated user position, and v_i is the white noise. The whole measurement equation is given as follows:

$$z_{gps} = H_{gps} x_{gps} + v_{gps} \quad (2)$$

where $z_{gps} = [z_1 \ z_2 \ \dots \ z_m]'$, $H_{gps} = [H'_1 \ H'_2 \ \dots \ H'_m]'$, $v_{gps} = [v_1 \ v_2 \ \dots \ v_m]'$.

From the dynamic Equation (1) and the measurement (2), the accelerations \ddot{x} , \ddot{y} , and \ddot{z} can be estimated using the Kalman filter [21].

2.3. AHRS

AHRS provides the attitude and heading and thus, the direction cosine matrix C_b^n can be calculated uniquely if the rotation sequence of roll, pitch, and heading is pre-defined. Many approaches have been proposed for AHRS [22–25] using accelerometer, gyroscope, and magnetometer. Accelerometers provide roll and pitch, and magnetometers provide heading. Hence the roll, pitch, and heading obtained from accelerometers and magnetometers can be compared with those from the gyroscope, and thus the Kalman filter can be used to estimate attitude and heading.

In many cases, quaternion is used to avoid deadlock and to save time. Quaternion q is defined as one scalar and a three- or four-dimensional vector as follows:

$$q = q_0 + q_1 i + q_2 j + q_3 k = [q_0 \ q_1 \ q_2 \ q_3]'$$

The direction cosine matrix C_b^n is related with the quaternion q as in (3).

$$C_b^n = \begin{bmatrix} q_0^2 + q_1^2 - q_2^2 - q_3^2 & 2(q_1 q_2 + q_0 q_3) & 2(q_1 q_3 - q_0 q_2) \\ 2(q_1 q_2 - q_0 q_3) & q_0^2 - q_1^2 + q_2^2 - q_3^2 & 2(q_2 q_3 + q_0 q_1) \\ 2(q_1 q_3 + q_0 q_2) & 2(q_2 q_3 - q_0 q_1) & q_0^2 - q_1^2 - q_2^2 + q_3^2 \end{bmatrix} \quad (3)$$

The quaternion q is updated as the following differential equation

$$\dot{q} = \frac{1}{2} W q$$

$$\text{where } W = \begin{bmatrix} 0 & -\omega_x & -\omega_y & -\omega_z \\ \omega_x & 0 & \omega_z & -\omega_y \\ \omega_y & -\omega_z & 0 & \omega_x \\ \omega_z & \omega_y & -\omega_x & 0 \end{bmatrix}.$$

The direction cosine matrix \hat{C}_b^n , which is the output of AHRS, can be described as

$$\hat{C}_b^n = (I + \Psi) C_b^n$$

where C_b^n is the true direction cosine matrix, and Ψ denotes the orientation error of AHRS and is a skew symmetric matrix as follows:

$$\Psi = \begin{bmatrix} 0 & -\delta\psi & \delta\theta \\ \delta\psi & 0 & -\delta\phi \\ -\delta\theta & \delta\phi & 0 \end{bmatrix}, \begin{bmatrix} \delta\phi \\ \delta\theta \\ \delta\psi \end{bmatrix} = \begin{bmatrix} \delta\phi \sim N(0, \sigma_\phi^2) \\ \delta\theta \sim N(0, \sigma_\theta^2) \\ \delta\psi \sim N(0, \sigma_\psi^2) \end{bmatrix} \quad (4)$$

where ϕ is roll, θ is pitch, and ψ is heading. As discussed in Section 2.1, it is assumed that IMU calibration and initial alignment is performed in advance before AHRS block as in Figure 1. Thus deterministic and some random errors are compensated in the IMU calibration and initial alignment block. Then the remaining orientation error $\delta\phi$, $\delta\theta$, and $\delta\psi$ can be assumed to have Gaussian distribution as in (4).

3. Definition of the Decision Variables and the Structure of the Second-half of the Proposed Direct GPS Spoofing Detection

This section describes the acceleration error equation for the direct GPS spoofing detection and defines two decision variables to decide whether a spoofing signal exists or not. One decision variable is the magnitude of the horizontal acceleration error and the other is the magnitude of the north (or east) direction acceleration error. The probability density functions and the thresholds for spoofing detection are given for the two decision variables.

3.1. Acceleration Error Equation

The acceleration estimated from the GPS receiver is described as follows,

$$\hat{f}_{gps}^n = f_{gps}^n + \epsilon_{gps}^n \quad (5)$$

where f_{gps}^n is the true moving acceleration (plus spoofing acceleration if any) in the navigation frame and ϵ_{gps}^n is the white noise.

The specific force measured from the accelerometers \hat{f}_{acc}^b in the body frame is transformed into the navigation frame \hat{f}_{acc}^n by using the direction cosine matrix \hat{C}_b^n obtained from the AHRS as follows,

$$\hat{f}_{acc}^n = \hat{C}_b^n \hat{f}_{acc}^b = (C_b^n + \Psi C_b^n)(f_{acc}^b + \epsilon_{acc}^b) \approx f_{acc}^n + \Psi f_{acc}^n + \epsilon_{acc}^n \quad (6)$$

where f_{acc}^n is the true specific force, Ψ is defined in (4), and ϵ_{acc}^n is the white noise of accelerometers. The Coriolis effect is assumed to be negligible with the assumption of low moving velocity for brevity. Notice that the z-component of f_{acc}^n contains the gravity.

The acceleration error equation is described from the difference of \hat{f}_{gps}^n and \hat{f}_{acc}^n as follows:

$$z = \hat{f}_{gps}^n - \hat{f}_{acc}^n \quad (7)$$

3.2. Decision Variable z_{mag} as the Magnitude of the Horizontal Acceleration Error

Suppose that the hypothesis H_0 denotes the case of the absence of the spoofing signal, and H_1 denotes the case of the presence of the spoofing signal. For hypothesis H_0 , the acceleration error is denoted as z_0 , and for hypothesis H_1 , the acceleration error is denoted as z_1 . Then, z_0 and z_1 can be described from Equations (5) and (6) as follows:

$$z_0 = \hat{f}_{gps}^n - \hat{f}_{acc}^n = \epsilon_{gps}^n - \Psi f_{acc}^n - \epsilon_{acc}^n = \begin{bmatrix} z_{0n} \\ z_{0e} \\ z_{0d} \end{bmatrix} \quad (8)$$

$$\begin{aligned} z_1 &= \hat{f}_{gps,spoofed}^n - \hat{f}_{acc}^n = f_s^n + \epsilon_{gps}^n - \Psi f_{acc}^n - \epsilon_{acc}^n \\ &= \begin{bmatrix} f_{s,n}^n + \epsilon_{gps,n}^n - \delta\psi f_{acc,e}^n + \delta\theta f_{acc,d}^n - \epsilon_{acc,n}^n \\ f_{s,e}^n + \epsilon_{gps,e}^n + \delta\psi f_{acc,n}^n - \delta\phi f_{acc,d}^n - \epsilon_{acc,e}^n \\ f_{s,d}^n + \epsilon_{gps,d}^n - \delta\theta f_{acc,n}^n + \delta\phi f_{acc,e}^n - \epsilon_{acc,d}^n \end{bmatrix} = \begin{bmatrix} z_{1n} \\ z_{1e} \\ z_{1d} \end{bmatrix} \end{aligned} \quad (9)$$

where $f_{s,n}^n$, $f_{s,e}^n$, $f_{s,d}^n$ are north, east, down components of spoofing acceleration.

Only the x , y components of the acceleration error equation (8), (9) are used in this study. The acceleration errors z_0 and z_1 are expressed in the navigation frame and the superscript n will be omitted henceforth, for brevity.

In Equation (9), the random variables z_{1n} and z_{1e} , which are north and east components of z_1 , have Gaussian distribution and the probability density function (PDF) is as follows,

$$z_{1n} : f_{Z_{1n}}(z) = \frac{1}{\sqrt{2\pi}\sigma_n} e^{-\frac{(z-f_{s,n})^2}{2\sigma_n^2}} \text{ where } \sigma_n^2 = \epsilon_{gps,n}^2 + \sigma_\psi^2 f_{acc,e}^2 + \sigma_\theta^2 f_{acc,d}^2 + \epsilon_{acc,n}^2 \quad (10)$$

$$z_{1e} : f_{Z_{1e}}(z) = \frac{1}{\sqrt{2\pi}\sigma_e} e^{-\frac{(z-f_{s,e})^2}{2\sigma_e^2}} \text{ where } \sigma_e^2 = \epsilon_{gps,e}^2 + \sigma_\psi^2 f_{acc,n}^2 + \sigma_\phi^2 f_{acc,d}^2 + \epsilon_{acc,e}^2 \quad (11)$$

3.2.1. Probability Density Function of the Magnitude of the Horizontal Acceleration Error z_{mag}

z_{1mag} is defined as the magnitude of the horizontal component of z_1 as follows:

$z_{1mag} = \sqrt{z_{1n}^2 + z_{1e}^2}$, where $z_{1n} \sim N(f_{s,n}, \sigma_n^2)$ and $z_{1e} \sim N(f_{s,e}, \sigma_e^2)$ with σ_n^2 and σ_e^2 being defined in (10) and (11).

The variances σ_n^2 and σ_e^2 have different values and depend on the AHRS attitude accuracy times moving acceleration. Thus σ_n^2 and σ_e^2 are time-varying if the moving acceleration varies with time.

The PDF of the z_{1mag} could not be found in the literature and thus it was derived in this paper and called as Shim PDF. Lemma 1 shows the PDF of z_{1mag} .

Lemma 1. (Shim PDF) Consider the independent Gaussian random variables X and Y with $X \sim N(m_1, \sigma_1^2)$ and $Y \sim N(m_2, \sigma_2^2)$. Then, the magnitude $Z = \sqrt{X^2 + Y^2}$ has the following PDF:

$$f_Z(z) = \frac{z}{\sigma_1\sigma_2} \exp\left[-\frac{1}{4}\left(\frac{1}{\sigma_1^2} + \frac{1}{\sigma_2^2}\right)(z^2 + \alpha^2)\right] I_1(z), \quad z \geq 0 \quad (12)$$

$$\begin{aligned} \text{where } I_1(z) &= \frac{1}{2\pi} \int_0^{2\pi} \exp\left[\frac{1}{4}\left(\frac{1}{\sigma_2^2} - \frac{1}{\sigma_1^2}\right)z^2 \cos(2\theta) + \sqrt{\left(\frac{m_1}{\sigma_1^2}\right)^2 + \left(\frac{m_2}{\sigma_2^2}\right)^2} \cdot z \cos(\theta - \phi)\right] d\theta, \quad \text{and } \alpha^2 = \\ &\frac{2(\sigma_2^2 m_1^2 + \sigma_1^2 m_2^2)}{\sigma_1^2 + \sigma_2^2} = \frac{2\left(\frac{m_1^2}{\sigma_1^2} + \frac{m_2^2}{\sigma_2^2}\right)}{\frac{1}{\sigma_1^2} + \frac{1}{\sigma_2^2}}, \quad \phi = \tan^{-1}\left(\frac{m_2\sigma_1^2}{m_1\sigma_2^2}\right) = \tan^{-1}\left(\frac{\frac{m_2}{\sigma_2^2}}{\frac{m_1}{\sigma_1^2}}\right). \end{aligned}$$

Proof. The variable change for the independent Gaussian random variables X and Y is as

$$U = \frac{X}{s}, V = \frac{Y}{s} \text{ where } U \sim N\left(\frac{m_1}{s}, \frac{\sigma_1^2}{s^2}\right), V \sim N\left(\frac{m_2}{s}, \frac{\sigma_2^2}{s^2}\right) \text{ and } s = \sqrt{\sigma_1^2 + \sigma_2^2}$$

Defining $\mu_1 = \frac{m_1}{s}$ and $\mu_2 = \frac{m_2}{s}$, $b = \frac{\sigma_1^2 - \sigma_2^2}{\sigma_1^2 + \sigma_2^2}$, it can be understood that $U \sim N\left(\mu_1, \frac{1+b}{2}\right)$, $V \sim N\left(\mu_2, \frac{1-b}{2}\right)$ and $-1 \leq b \leq 1$.

The idea of using s and b above comes from Hoyt's paper [26]. Consider the joint PDF $f_{UV}(u, v)$.

$$\begin{aligned} f_{UV}(u, v) = f_U(u)f_V(v) &= \frac{1}{\sqrt{\pi(1+b)}} \exp\left[-\frac{(u-\mu_1)^2}{1+b}\right] \cdot \frac{1}{\sqrt{\pi(1-b)}} \exp\left[-\frac{(v-\mu_2)^2}{1-b}\right] \\ &= \frac{1}{\pi\sqrt{1-b^2}} \exp\left[-\frac{(u-\mu_1)^2}{1+b} - \frac{(v-\mu_2)^2}{1-b}\right] \end{aligned}$$

Defining $R = \sqrt{U^2 + V^2}$, the PDF $f_R(r)$ can be obtained as follows:

$$\begin{aligned} f_R(r) &= \int_0^{2\pi} f_{UV}(u, v) r d\theta \\ &= \int_0^{2\pi} f_{UV}(r \cos \theta, r \sin \theta) r d\theta \\ &= \int_0^{2\pi} \frac{1}{\pi\sqrt{1-b^2}} \exp\left[-\frac{(r \cos \theta - \mu_1)^2}{1+b} - \frac{(r \sin \theta - \mu_2)^2}{1-b}\right] r d\theta \end{aligned}$$

By algebraic manipulation of the above equation, $f_R(r) = \frac{r}{\pi\sqrt{1-b^2}} \exp\left[-\frac{r^2+\beta^2}{1-b^2}\right] \int_0^{2\pi} \exp\left[\frac{br^2 \cos(2\theta) + rA \cos(\theta - \phi)}{1-b^2}\right] d\theta$ where $\beta^2 = (1-b)\mu_1^2 + (1+b)\mu_2^2$, $A = 2\sqrt{(1-b)^2\mu_1^2 + (1+b)^2\mu_2^2}$, $\phi = \tan^{-1}\left(\frac{(1+b)\mu_2}{(1-b)\mu_1}\right)$.

From the relation between random variables Z and R as $Z = sR$, the PDF of Z can be obtained from $f_Z(z) = \frac{1}{s}f_R\left(\frac{z}{s}\right)$ as:

$$f_Z(z) = \frac{1}{s} \cdot \frac{z/s}{\pi\sqrt{1-b^2}} \exp\left[-\frac{\left(\frac{z}{s}\right)^2 + \beta^2}{1-b^2}\right] \int_0^{2\pi} \exp\left[\frac{b\left(\frac{z}{s}\right)^2 \cos(2\theta) + \left(\frac{z}{s}\right)A \cos(\theta - \phi)}{1-b^2}\right] d\theta \quad (13)$$

From algebraic manipulation of Equation (13), $\frac{1}{s} \cdot \frac{\frac{z}{s}}{\pi\sqrt{1-b^2}} = \frac{z}{\sigma_1\sigma_2 \cdot 2\pi}$ and $\exp\left[-\frac{\left(\frac{z}{s}\right)^2 + \beta^2}{1-b^2}\right] = \exp\left[-\frac{1}{4}\left(\frac{1}{\sigma_1^2} + \frac{1}{\sigma_2^2}\right)(z^2 + \alpha^2)\right]$ is obtained, and the integral term in Equation (13) becomes the integral term of $I_1(z)$, which results in Equation (12). \square

Rayleigh PDF and Rice PDF are well-known PDFs as the relation to Gaussian, and those two PDFs are special cases of Equation (12), which becomes Rayleigh PDF with the condition of $m_1 = m_2 = 0$ and $\sigma_1 = \sigma_2$, and becomes Rice PDF with the condition of $\sigma_1 = \sigma_2$.

Defining z_{0mag} as the magnitude of the horizontal component of z_0 as follows, $z_{0mag} = \sqrt{z_{0n}^2 + z_{0e}^2}$, where $z_{1n} \sim N(0, \sigma_n^2)$, $z_{1e} \sim N(0, \sigma_e^2)$.

The PDF of z_{0mag} can be obtained from Lemma 1 with $m_1 = m_2 = 0$ and the result is shown in Corollary 2.

Corollary 2. Consider the independent Gaussian random variables X and Y with $X \sim N(0, \sigma_1^2)$ and $Y \sim N(0, \sigma_2^2)$. Then the magnitude $Z = \sqrt{X^2 + Y^2}$ has the following PDF:

$$f_Z(z) = \frac{z}{\sigma_1 \sigma_2} \exp\left[-\frac{1}{4}\left(\frac{1}{\sigma_1^2} + \frac{1}{\sigma_2^2}\right)z^2\right] I_0\left(\frac{1}{4}\left(\frac{1}{\sigma_2^2} - \frac{1}{\sigma_1^2}\right)z^2\right), z \geq 0 \quad (14)$$

where $I_0(z) = \frac{1}{\pi} \int_0^\pi e^{z \cos \theta} d\theta$,

Proof. Equation (14) can be obtained easily from the PDF in Equation (12) with $m_1 = m_2 = 0$ and manipulation in the $I_0(z)$ part. \square

Equation (14) can be found in Reference [27] without proof.

3.2.2. Threshold to Detect GPS Spoofing for the Decision Variable z_{mag}

In this study, the probability of false alarm is used to obtain the threshold for the detection of spoofing. The threshold γ_{mag} to detect GPS spoofing is defined according to the pre-defined probability of false alarm P_{fa} as follows :

$$\text{prob}\{z_{0mag} \geq \gamma_{mag}\} = \text{prob}\{z_{mag} \geq \gamma_{mag} | H_0\} = P_{fa} \quad (15)$$

where

$$z_{mag} = \sqrt{z_n^2 + z_e^2} \quad (16)$$

and the probability is calculated from the integral of equation (14) from γ_{mag} to infinity.

Whether a spoofing signal exists or not is decided by the following decision rule:

$$\begin{array}{c} H_1 \\ z_{mag} \gtrless \gamma_{mag} \\ H_0 \end{array}$$

The variable z_{mag} above is said to be a decision variable since it is used to decide whether there is a spoofing signal or not.

3.3. Decision Variable z_{absN} (or z_{absE}) as the Magnitude of the North (or East) Direction Acceleration Error

3.3.1. Probability Density Function of the Magnitude of The North (or East) Acceleration Error z_{absN} (or z_{absE})

Defining z_{1absN} and z_{0absN} as the magnitude of the north component of z_1 and z_0 , respectively, $z_{1absN} = |z_{1n}|$ and $z_{0absN} = |z_{0n}|$ (similarly, $z_{1absE} = |z_{1e}|$ and $z_{0absE} = |z_{0e}|$).

The PDF of z_{1absN} (or z_{1absE}) and z_{0absN} (or z_{0absE}) can be obtained as Equations (17) and (18), which are called folded Gaussian [28], since z_{1n} and z_{0n} have Gaussian density functions as $z_{1n} \sim N(f_{s,n}, \sigma_n^2)$ and $z_{0n} \sim N(0, \sigma_n^2)$.

$$f_{Z_{1absN}}(z) = \frac{1}{\sqrt{2\pi}\sigma_n} e^{-\frac{(z-f_{s,n})^2}{2\sigma_n^2}} + \frac{1}{\sqrt{2\pi}\sigma_n} e^{-\frac{(z+f_{s,n})^2}{2\sigma_n^2}}, z \geq 0 \quad (17)$$

$$f_{Z_{0absN}}(z) = \frac{2}{\sqrt{2\pi}\sigma_n} e^{-\frac{z^2}{2\sigma_n^2}}, z \geq 0 \quad (18)$$

3.3.2. Threshold to Detect GPS Spoofing for the Decision Variable z_{absN}

The threshold γ_{absN} to detect GPS spoofing is defined according to the pre-defined probability of false alarm P_{fa} as follows :

$$\text{prob}\{z_{0absN} \geq \gamma_{absN}\} = \text{prob}\{z_{absN} \geq \gamma_{absN} | H_0\} = P_{fa} \quad (19)$$

here

$$z_{absN} = |z_n| \quad (20)$$

and the probability is calculated from the integral of Equation (18) from γ_{absN} to infinity. Whether a spoofing signal exists or not is decided by the following decision rule:

$$\begin{array}{c} H_1 \\ z_{absN} \gtrless \gamma_{absN} \\ H_0 \end{array}$$

3.4. The Structure of the Second-Half of the Proposed Direct GPS Spoofing Detection

This subsection shows the structure of the proposed second-half of direct GPS spoofing detection method in Figure 2, which is drawn after the rightmost signal in Figure 1. The analysis of the proposed structure shown in Figure 2 will be given in Sections 4 and 5 in detail.

In Section 4, it will be observed that the decision variable z_{absN} (or z_{absE}) shows a higher detection probability than z_{mag} in the condition that both moving acceleration and spoofing acceleration head within roughly 25° from the north (or east). Section 5 shows that when DMSA is used for performance measure, the decision variable z_{absN} (or z_{absE}) shows a smaller DMSA than z_{mag} in the condition that both moving acceleration and spoofing acceleration head within roughly 25° from the north–south direction (or east–west direction). From these results, a direct GPS spoofing detection method is proposed as follows:

If any of the three decision variables z_{mag} , z_{absN} , and z_{absE} are larger than or equal to the corresponding thresholds, then a spoofing signal is declared to exist.

Note that the threshold $\gamma_{mag}(t)$, $\gamma_{absN}(t)$, and $\gamma_{absE}(t)$ in Figure 2 are time-varying, not constant. The threshold $\gamma_{mag}(t)$ is obtained from Equation (15) given the probability of false alarm P_{fa} , where the PDF is Equation (14) with $\sigma_1 = \sigma_n$ and $\sigma_2 = \sigma_e$. The north and east variances σ_n^2 and σ_e^2 given in Equations (10) and (11) contain the moving acceleration and thus σ_n^2 and σ_e^2 are time-varying, which is why $\gamma_{mag}(t)$ is time-varying. The threshold $\gamma_{absN}(t)$ is obtained from Equation (18) and the PDF contains σ_n , which is time-varying. Thus $\gamma_{absN}(t)$ depends on the moving acceleration and becomes time-varying. Similarly $\gamma_{absE}(t)$ is time-varying. The red line and arrow in Figure 2 means that the threshold $\gamma_{mag}(t)$, $\gamma_{absN}(t)$, and $\gamma_{absE}(t)$ depend on the moving acceleration \hat{f}_{acc}^n .

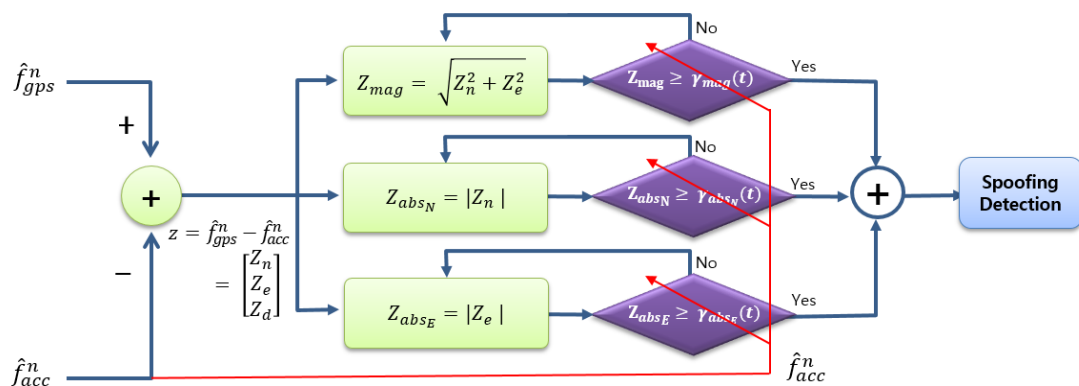


Figure 2. The Structure of the Second-half of the proposed direct GPS spoofing detection after Figure 1.

4. Performance Analysis of the Decision Variables using the Probability of Detection

This section shows the performance of the proposed direct GPS spoofing detection method for the two decision variables z_{mag} and z_{absN} (or z_{absE}) which are defined in Section 3.

4.1. Detection Threshold According to Moving Acceleration

Suppose that the probability of false alarm P_{fa} is pre-defined. Then, spoofing detection thresholds γ_{mag} and γ_{absN} (or γ_{absE}) are determined according to P_{fa} as in Equations (15) and (19). Taking the PDF Equations (14) and (18) into account, Equations (21) and (22) are obtained from Equations (15) and (19) to further obtain γ_{mag} and γ_{absN} .

$$\text{prob}\{z_{mag} \geq \gamma_{mag} | H_0\} = \int_{\gamma_{mag}}^{\infty} \frac{z}{\sigma_n \sigma_e} \exp\left[-\frac{1}{4}\left(\frac{1}{\sigma_n^2} + \frac{1}{\sigma_e^2}\right)z^2\right] I_0\left(\frac{1}{4}\left(\frac{1}{\sigma_e^2} - \frac{1}{\sigma_n^2}\right)z^2\right) dz = P_{fa} \quad (21)$$

$$\text{prob}\{z_{absN} \geq \gamma_{absN} | H_0\} = \int_{\gamma_{absN}}^{\infty} \frac{2}{\sqrt{2\pi}\sigma_n} e^{-\frac{z^2}{2\sigma_n^2}} dz = P_{fa} \quad (22)$$

where $\sigma_n^2 = \epsilon_{gps,n}^2 + \sigma_\psi^2 f_{acc,e}^2 + \sigma_\theta^2 f_{acc,d}^2 + \epsilon_{acc,n}^2$ and $\sigma_e^2 = \epsilon_{gps,e}^2 + \sigma_\psi^2 f_{acc,n}^2 + \sigma_\phi^2 f_{acc,d}^2 + \epsilon_{acc,e}^2$.

To see the detection performance result clearly, the vertical moving acceleration is supposed to be zero and the gravity is compensated before the acceleration error is obtained. Thus the following variances in Equation (23) are used in the simulation from now on.

$$\sigma_n^2 = \epsilon_{gps,n}^2 + \sigma_\psi^2 f_{acc,e}^2 + \epsilon_{acc,n}^2 \text{ and } \sigma_e^2 = \epsilon_{gps,e}^2 + \sigma_\psi^2 f_{acc,n}^2 + \epsilon_{acc,e}^2 \quad (23)$$

The detection thresholds γ_{mag} and γ_{absN} depend on the variances σ_n^2 and σ_e^2 which are functions of moving acceleration f_{acc} as in (23). Thus, the detection threshold γ_{mag} and γ_{absN} are not constant but vary according to the magnitude and direction of the moving acceleration f_{acc} . Figure 3 shows detection thresholds γ_{mag} and γ_{absN} according to the direction of f_{acc} with two cases of magnitude, (a) $|f_{acc}| = 0.2 \text{ m/s}^2$ and (b) $|f_{acc}| = 0.4 \text{ m/s}^2$. The threshold is the distance from the origin for the corresponding direction of f_{acc} . It is observed that for the same magnitude of moving acceleration, γ_{mag} has maximum values in the north and east directions and γ_{absN} has the minimum value in the north direction. Similarly, γ_{absN} has the minimum value in the east direction.

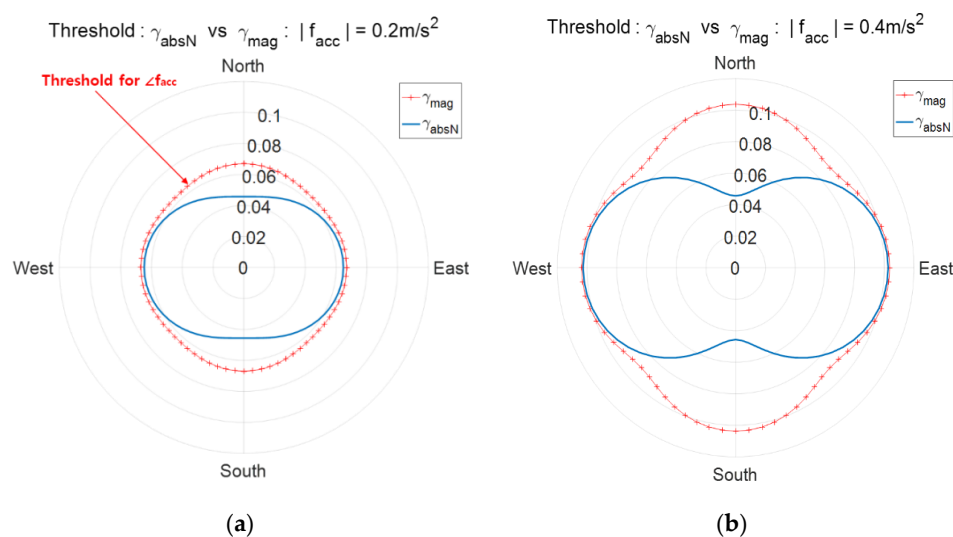


Figure 3. Spoofing detection thresholds γ_{mag} and γ_{absN} according to the moving acceleration. The distance from the origin is the threshold for the corresponding direction of moving acceleration; (a) $|f_{acc}| = 0.2 \text{ m/s}^2$, (b) $|f_{acc}| = 0.4 \text{ m/s}^2$.

4.2. Effects of Moving Acceleration on the Performance of Spoofing Detection

This subsection analyzes the effects of moving acceleration on the performance of spoofing detection. The effects of moving acceleration, magnitude and direction are separately examined, for both decision variables z_{mag} and z_{absN} which are defined in Section 3.

The probability of detection P_d is used for the performance of spoofing detection with the pre-defined probability of false alarm P_{fa} . When the detection threshold γ_{mag} and γ_{absN} are obtained from P_{fa} , the corresponding detection probabilities $P_{d,mag}$ and $P_{d,absN}$ are defined as follows:

$$P_{d,mag} = \text{prob}\{z_{mag} \geq \gamma_{mag} | H_1\} \text{ and } P_{d,absN} = \text{prob}\{z_{absN} \geq \gamma_{absN} | H_1\} \quad (24)$$

where the probability density functions (12) and (17) are integrated from the detection threshold to infinity.

4.2.1. Performance of Spoofing Detection According to the Magnitude of Moving Acceleration

The probability of detection P_d depends on both moving acceleration f_{acc} and spoofing acceleration f_s . The effect of the magnitude of moving acceleration is focused on in this subsection.

Suppose that the probability of the false alarm is pre-defined as $P_{fa} = 0.001$, the AHRS attitude accuracies of roll, pitch, and heading are 2° , 2° , and 4° , respectively, and moving acceleration is heading north. Figure 4 plots P_d according to the magnitude of f_s and shows that P_d increases as $|f_s|$ increases. The big arrow in cyan color in the upper left corner of Figure 4 denotes the moving acceleration f_{acc} and the narrow arrow in red color denotes the spoofing acceleration f_s . Figure 4a shows the case of both f_{acc} and f_s heading north, and plots four curves, two pink in color and two black in color, where the two pink curves show $P_{d,mag}$ and the two black curves show $P_{d,absN}$. The two black curves are same as one, implying that two cases of $|f_{acc}| = 0.1 \text{ m/s}^2$ and $|f_{acc}| = 0.2 \text{ m/s}^2$ do not cause any effect on $P_{d,absN}$, while the two pink curves show different results. As $|f_{acc}|$ changes from 0.1 m/s^2 to 0.2 m/s^2 , the performance of using z_{mag} , which is $P_{d,mag}$, deteriorates. Figure 4a shows that the performance of using z_{absN} is always better than that of using z_{mag} when both f_{acc} and f_s head north. Figure 4b shows similar results as Figure 4a when f_s heads 20° east from north.

The reason the two black curves are the same in Figure 4 despite two different $|f_{acc}|$ s is because the variance σ_n^2 in (10) does not contain $f_{acc,n}$, but $f_{acc,e}$. When f_{acc} heads north, $f_{acc,e} = 0$ and thus for a different north speed, the threshold γ_{absN} is same, which provides the same $P_{d,absN}$.

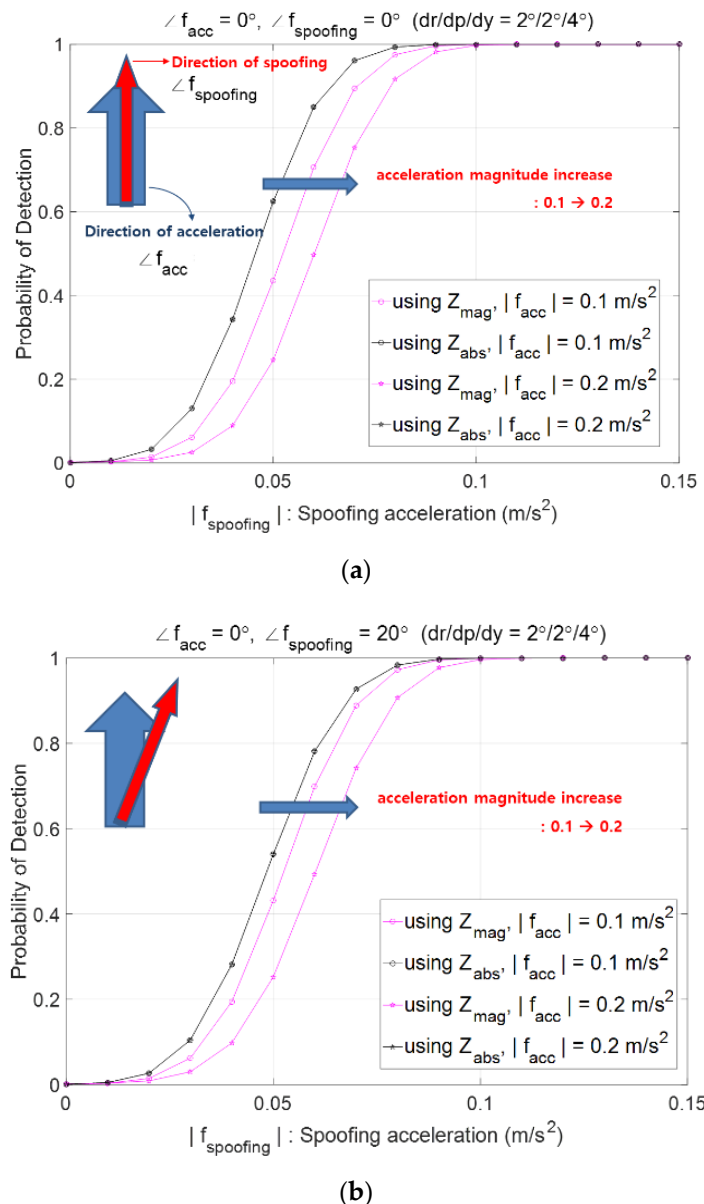


Figure 4. Probabilities of spoofing detection, $P_{d,mag}$ and $P_{d,absN}$ when (a) Both f_{acc} and f_s are heading north, (b) f_{acc} is heading north and f_s heading northeast 20° (arrow in cyan: moving acceleration f_{acc} , narrow arrow in red: spoofing acceleration f_s).

4.2.2. Performance of Spoofing Detection According to the Direction of Moving Acceleration

In this subsection, the effect of the direction of moving acceleration on the spoofing detection performance is presented. When the direction of f_{acc} changes from north to northeast of 30°, Figure 4a changes into Figure 5, where two black curves are distinct. Since the direction of f_{acc} changes from north to northeast of 30°, the east component $f_{acc,e}$ exists and thus σ_n^2 is different for different speeds, which results in a different threshold γ_{absN} and thus different $P_{d,absN}$. For both Z_{mag} and Z_{absN} the performance P_d deteriorates as $|f_{acc}|$ increases from 0.1 m/s² to 0.2 m/s². Looking into the black curve of $|f_{acc}| = 0.1 \text{ m/s}^2$ carefully in Figures 4a and 5, it is observed that $P_{d,absN}$ with f_{acc} heading north is bigger than $P_{d,absN}$ with f_{acc} heading northeast of 30°. For both Figures 4 and 5, the performance of $P_{d,absN}$ is better than that of $P_{d,mag}$.

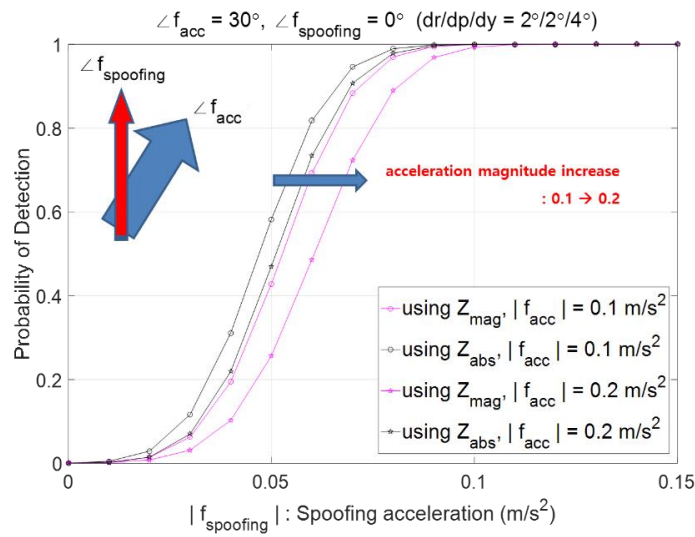


Figure 5. Probability of spoofing detection, $P_{d,mag}$ and $P_{d,absN}$ when f_{acc} heads northeast.

4.3. Effects of Spoofing Acceleration on the Performance of Spoofing Detection

This subsection analyzes the effects of spoofing acceleration on the performance of spoofing detection. The effects of the direction of the spoofing acceleration are examined for both decision variables z_{mag} and z_{absN} .

Figure 6 shows the spoofing detection probability when spoofing direction changes from 0° to 40° from north in the case of f_{acc} heading north as (a) and heading 30° east from north as (b). The horizontal axis is the magnitude of spoofing acceleration. It shows that $P_{d,mag}$ does not depend on the direction of spoofing acceleration while $P_{d,absN}$ decreases as the spoofing direction changes from 0° to 40° from north. This is because the north component of spoofing acceleration decreases as the spoofing direction gets far away from the north. It is observed that $P_{d,absN}$ is greater than $P_{d,mag}$ when the direction of f_s is less than 20° for both Figure 6a,b.

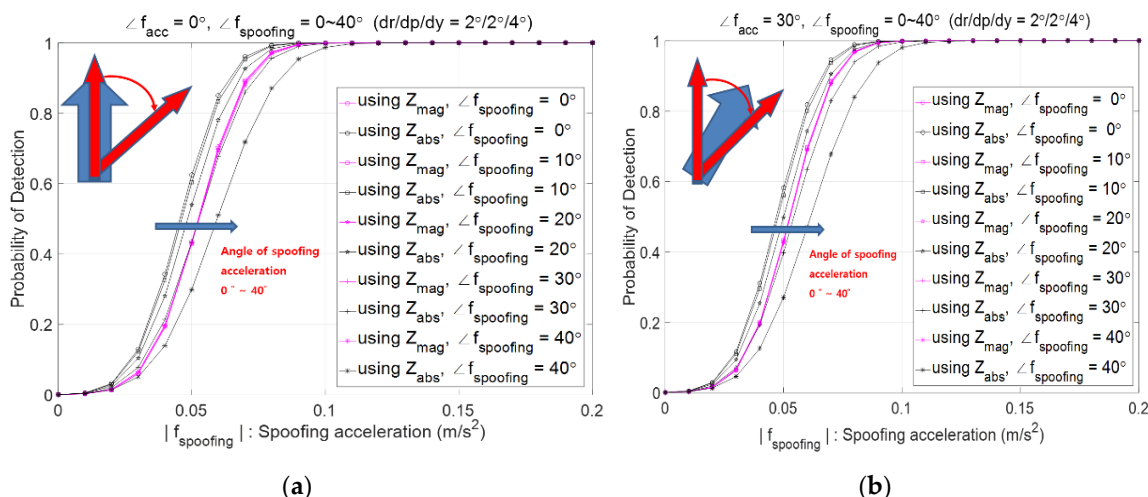


Figure 6. Probability of spoofing detection, $P_{d,mag}$ and $P_{d,absN}$ according to $\angle f_s$ with $|f_{acc}| = 0.6 \text{ m/s}^2$, where f_s is red color and f_{acc} is cyan color; (a) f_{acc} is heading north, (b) f_{acc} is heading 30° east from north.

4.4. Effects of Sensor Accuracy on the Performance of Spoofing Detection

This subsection analyzes the effects of sensor accuracy on the performance of spoofing detection. Figure 7a considers AHRS accuracies of 2° , 2° , and 4° for the roll, pitch, and heading errors while Figure 7b considers AHRS accuracies of 1° , 1° , and 2° . It is observed that $P_{d,mag}$ (pink color) decreases as the magnitude of f_{acc} increases or AHRS accuracy deteriorates. When both f_{acc} and f_s head north, $P_{d,absN}$ is greater than $P_{d,mag}$ in Figure 7. Better the AHRS accuracy, the better is the spoofing detection performance and this can be explained in Figure 8 which shows that with better AHRS accuracy, the threshold is smaller, which results in higher detection performance.

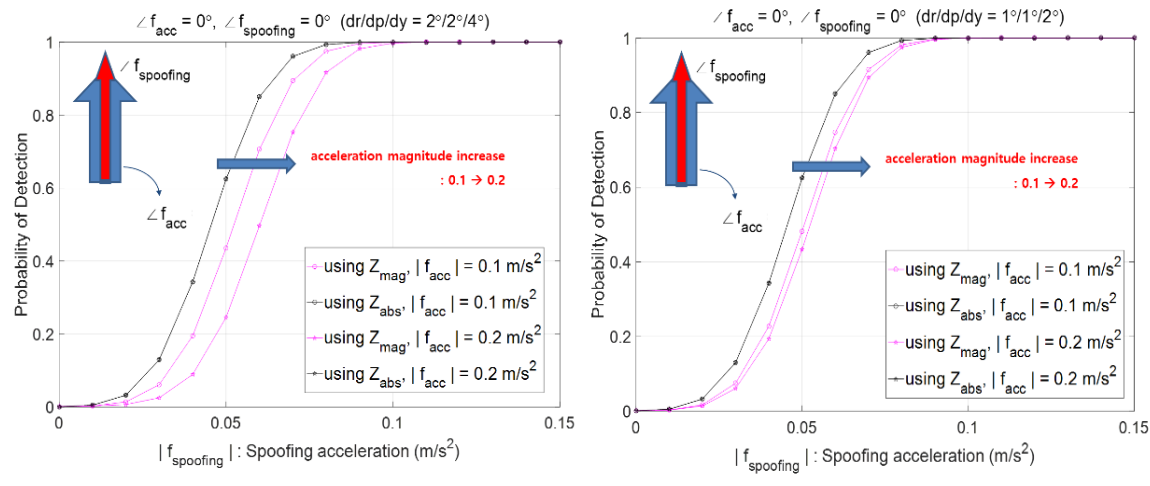


Figure 7. Probability of spoofing detection, $P_{d,mag}$ and $P_{d,absN}$ according to Attitude and Heading Reference System (AHRS) accuracy.

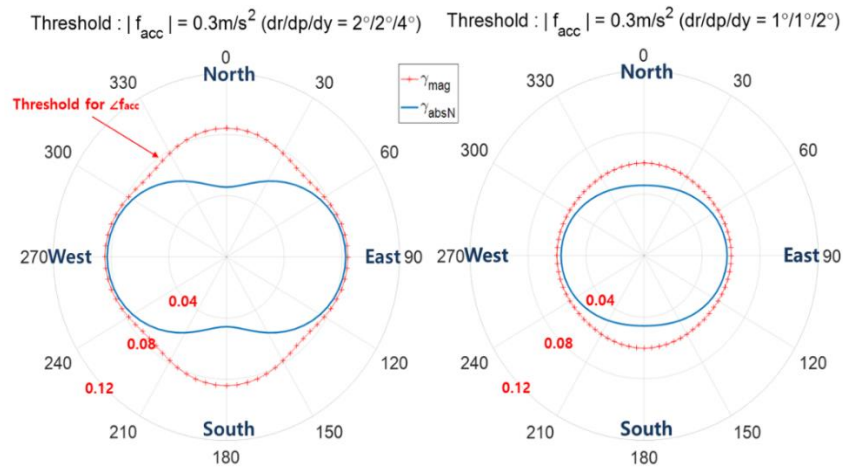


Figure 8. Comparison of spoofing detection threshold according to AHRS accuracy - the angles denote the direction of f_{acc} , i.e., $\angle f_{acc}$.

5. Performance Analysis of the Decision Variables Using the Detectable Minimum Spoofing Acceleration (DMSA)

This section compares the performance of the proposed direct GPS spoofing detection method for the two decision variables z_{mag} and z_{absN} (or z_{absE}) using the minimum threshold of spoofing detection with pre-defined false alarm probability and detection probability.

5.1. Spoofing Detection Threshold According to Moving Acceleration

The detection threshold γ_{mag} and γ_{absN} according to the direction of f_{acc} for the two cases of $|f_{acc}| = 0.2 \text{ m/s}^2$ and $|f_{acc}| = 0.4 \text{ m/s}^2$ are shown in Figure 3, where two decision variables z_{mag} and z_{absN} are used. Figure 9 shows Figure 3a,b together again upon adding the case of $|f_{acc}| = 0.6 \text{ m/s}^2$ under the condition of $P_{fa} = 0.001$ and the AHRS attitude accuracy of $2/2/4^\circ$. Figure 9 shows the exact threshold γ_{mag} and γ_{absN} and is obtained using Equations (21) and (22) given the pre-defined p_{fa} .

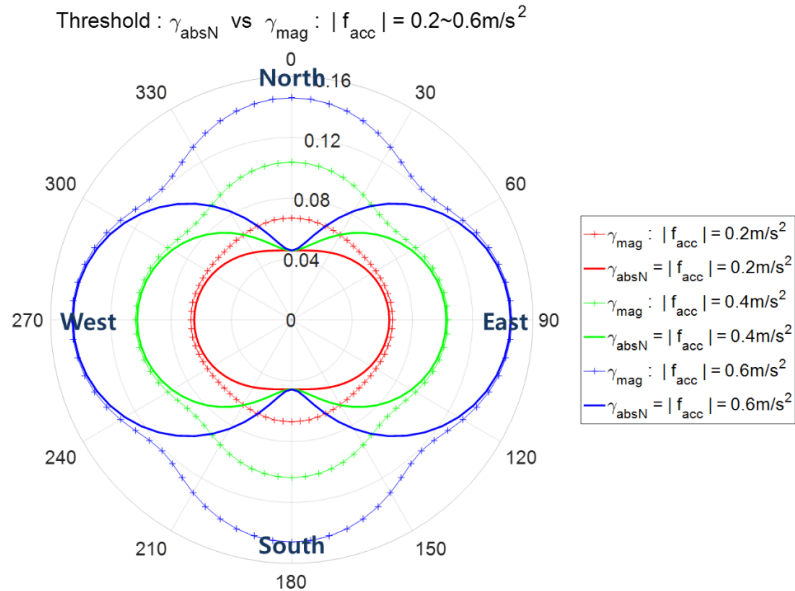


Figure 9. The threshold of spoofing detection γ_{mag} and γ_{absN} according to f_{acc} , the angle denotes the direction of f_{acc} , i.e., $\angle f_{acc}$.

5.2. Definition of DMSA

This section defines the detectable minimum spoofing acceleration (DMSA) and compares the DMSA for the decision variables z_{mag} and z_{absN} .

DMSA is the magnitude of the minimum spoofing acceleration to obtain a pre-defined detection probability P_d given a pre-defined false alarm probability P_{fa} . $P_{fa} = 0.001$, $P_d = 0.99$, and AHRS attitude accuracy of $2/2/4^\circ$ are used for DMSA in the simulations. Figure 10 shows an example of the computation results of DMSA, where the big arrow in cyan color is the moving acceleration f_{acc} and the angles of 0 through 360° denote the angle of spoofing acceleration f_s . The contour of red '+' is the set of DMSA for all directions of f_s . For example, the 'x' point means that when f_s comes from 330° direction, the DMSA is the distance from the origin to 'x' point, which guarantees $P_d = 0.99$.

5.2.1. Contour of DMSA Using The Decision Variable z_{mag} Depending on The Moving Acceleration

For a given DMSA in Figure 10, the values of P_{fa} , P_d , and AHRS attitude accuracy are fixed in advance, and thus the moving acceleration is the only remaining parameter that can affect the DMSA. Figure 11a–c show the contour of DMSA according to $\angle f_{acc}$ of 0° , 30° , and 45° . Greater the $|f_{acc}|$, the bigger the DMSA. The contour of DMSA in Figure 11c appears like a circle since the north and east component of f_{acc} are same and thus $\sigma_n = \sigma_e$. To check the effect of the AHRS accuracy, the DMSA is calculated for two sets of AHRS attitude accuracy of $1/1/2^\circ$ and $2/2/4^\circ$ in Figure 11d which shows that the better the accuracy, the smaller the contour of DMSA.

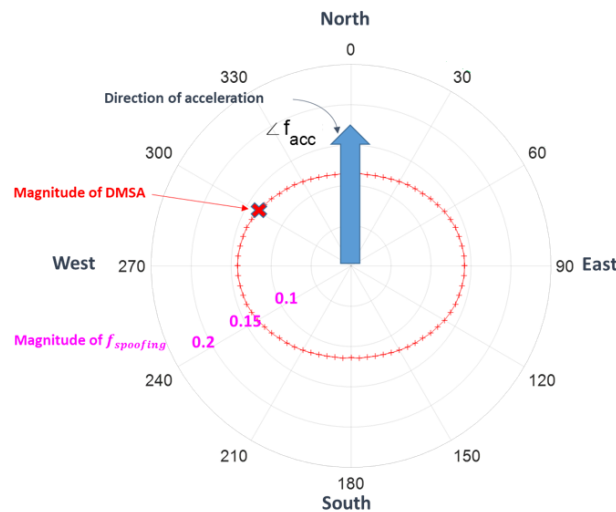


Figure 10. Detectable minimum spoofing acceleration (DMSA), the angle denotes the direction of f_s , i.e., $\angle f_s$.

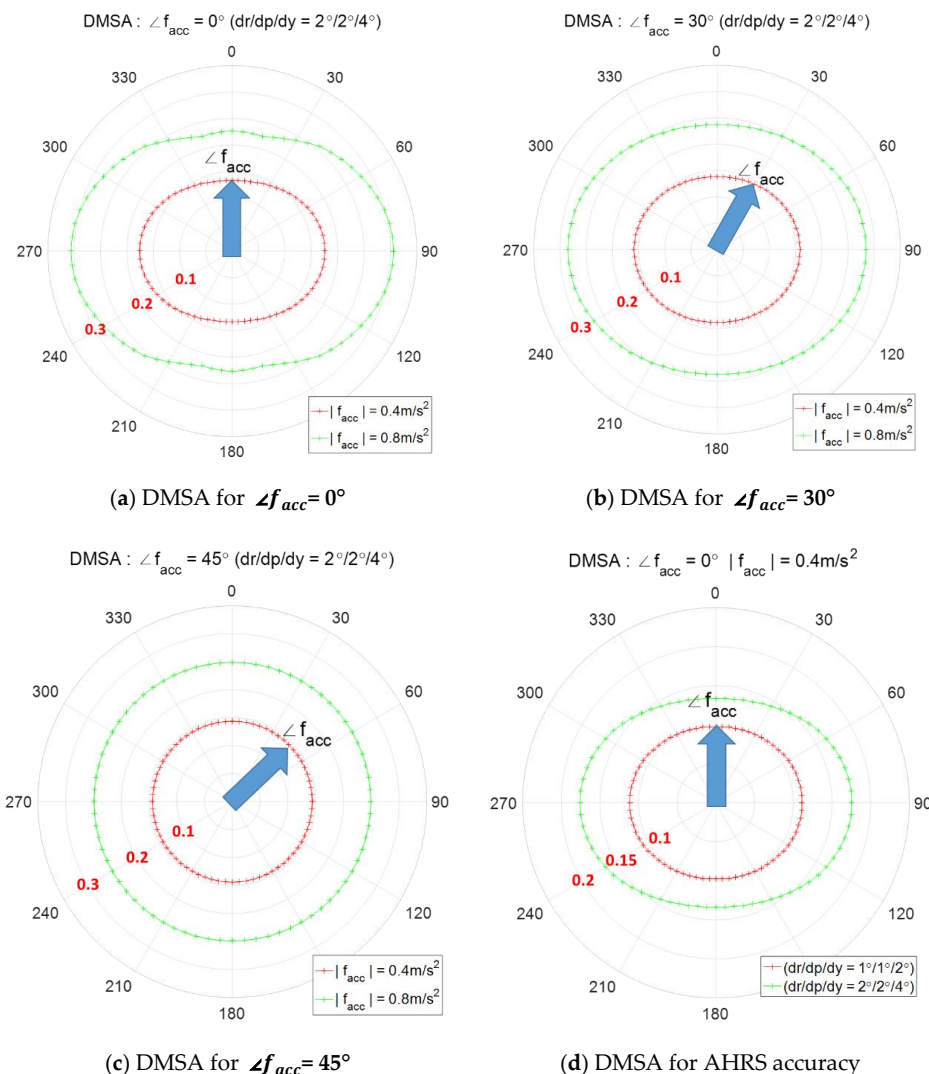


Figure 11. Contour of DMSA using the decision variable z_{mag} , the angle denotes the direction of f_s , i.e., $\angle f_s$; (a) $\angle f_{acc} = 0^\circ$, (b) $\angle f_{acc} = 30^\circ$, (c) $\angle f_{acc} = 45^\circ$, and (d) AHRS accuracy.

5.2.2. Contour of DMSA Using The Decision Variable Z_{absN} Depending on the Moving Acceleration

This subsection shows the contour of DMSA for the decision variable $Z_{absN} = |z_n|$. Figure 12 shows the contour of DMSA for $\angle f_{acc} = 0^\circ$. When f_{acc} heads north, the variance σ_n does not depend on $|f_{acc}|$ as shown in Figure 9, so the threshold and DMSA are the same for different magnitudes of f_{acc} as in Figure 12a,b. The contour of DMSA is a line passing through the minimum point of the north direction. Figure 13 shows the contour of DMSA for $\angle f_{acc} = 30^\circ$. In this case, the east component of f_{acc} has an effect on the σ_n , which results in a different threshold and DMSA according to different $|f_{acc}|$ as in Figure 13. The bigger the acceleration, the bigger is the DMSA.

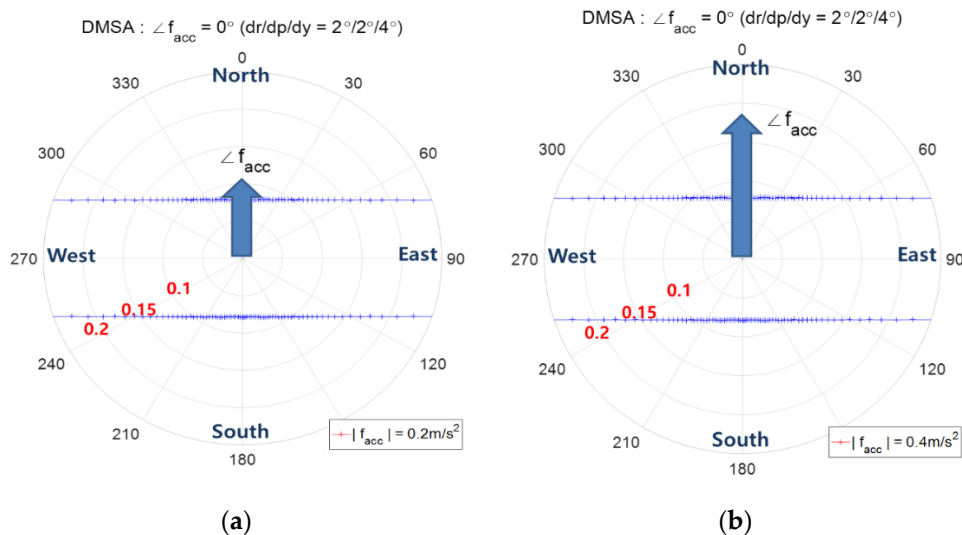


Figure 12. Contour of DMSA using the decision variable z_{absN} ($\angle f_{acc} = 0^\circ$), the angle denotes the direction of f_s , i.e., $\angle f_s$; (a) $|f_{acc}| = 0.2\text{m/s}^2$ (b) $|f_{acc}| = 0.4\text{m/s}^2$.

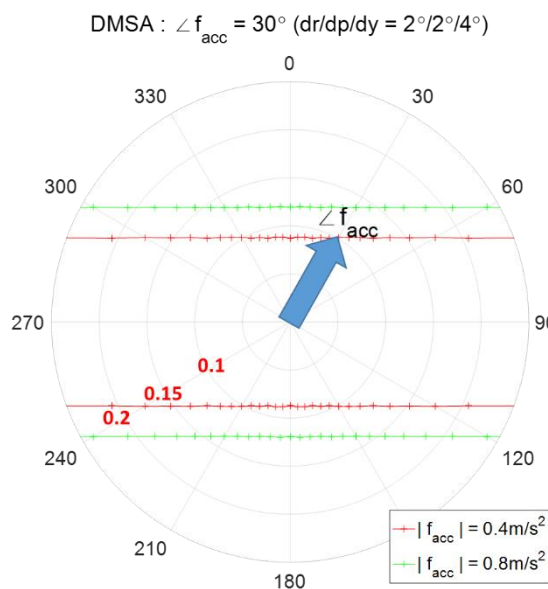


Figure 13. Contour of DMSA using the decision variable Z_{absN} ($\angle f_{acc} = 30^\circ$), the angle denotes the direction of f_s , i.e., $\angle f_s$.

5.3. Optimal Combined Contour of DMSA Using Both z_{mag} and z_{absN} (or z_{absE})

When both decision variables z_{mag} and z_{absN} (or z_{absE}) are used, the optimal combined contour can be obtained by combining Figures 11 and 12. Here, the optimal combined contour, colored in pink, is the

inner most combined contour from the two contours of DMSA using z_{mag} and z_{absN} . Figure 14a shows the optimal combined contour in the case of $|f_{acc}| = 0.2 \text{ m/s}^2$ and $\angle f_{acc} = 0^\circ$. When the magnitude is increased to $|f_{acc}| = 0.4 \text{ m/s}^2$ while maintaining the direction, Figure 14b shows that the threshold γ_{mag} is increased, but the threshold γ_{absN} does not change. In Figure 14a,b, it is observed that when f_{acc} heads north, as $|f_{acc}|$ increases, the difference $\gamma_{mag} - \gamma_{absN}$ becomes larger and the range of angles where $DMSA_{absN} < DMSA_{mag}$ holds, becomes larger. Figure 14c,d show the case of $\angle f_{acc} = 30^\circ$ and $\angle f_{acc} = 90^\circ$, respectively. When f_{acc} heads east, i.e., $\angle f_{acc} = 90^\circ$ as in Figure 14d, z_{absE} and γ_{absN} should be used instead of z_{absN} and γ_{absN} .

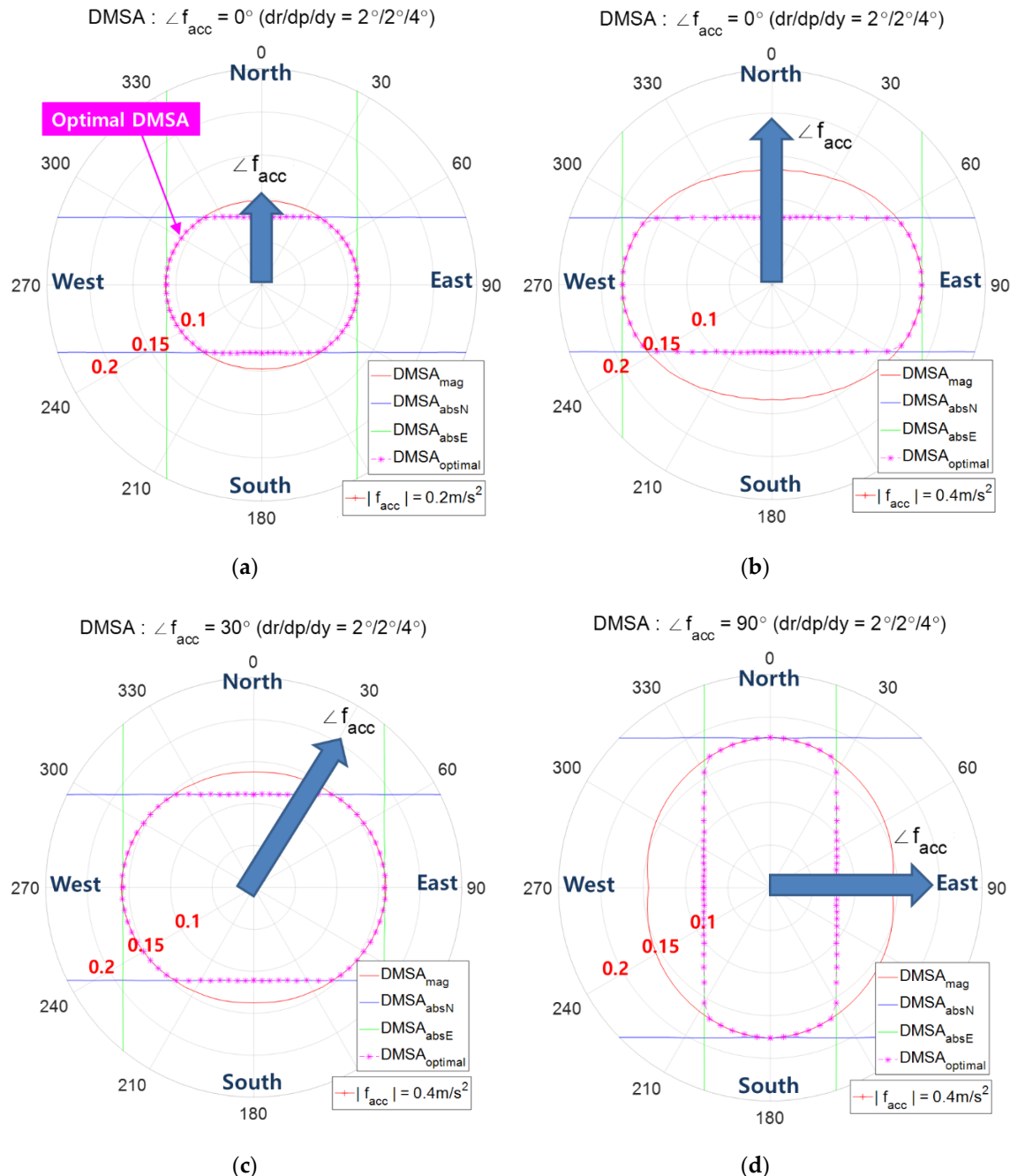


Figure 14. Optimal combined contour (pink color) of DMSA using both z_{mag} and z_{absN} , the angle denotes the direction of f_s , i.e., $\angle f_s$; (a) $\angle f_{acc} = 0^\circ$, $|f_{acc}| = 0.2 \text{ m/s}^2$, (b) $\angle f_{acc} = 0^\circ$, $|f_{acc}| = 0.4 \text{ m/s}^2$, (c) $\angle f_{acc} = 30^\circ$, $|f_{acc}| = 0.4 \text{ m/s}^2$, and (d) $\angle f_{acc} = 90^\circ$, $|f_{acc}| = 0.4 \text{ m/s}^2$.

Figure 15 shows the combined contour of DMSA using both z_{mag} and z_{absN} according to the AHRS attitude accuracy. It shows that as the attitude accuracy enhances, the combined contour of DMSA shrinks.

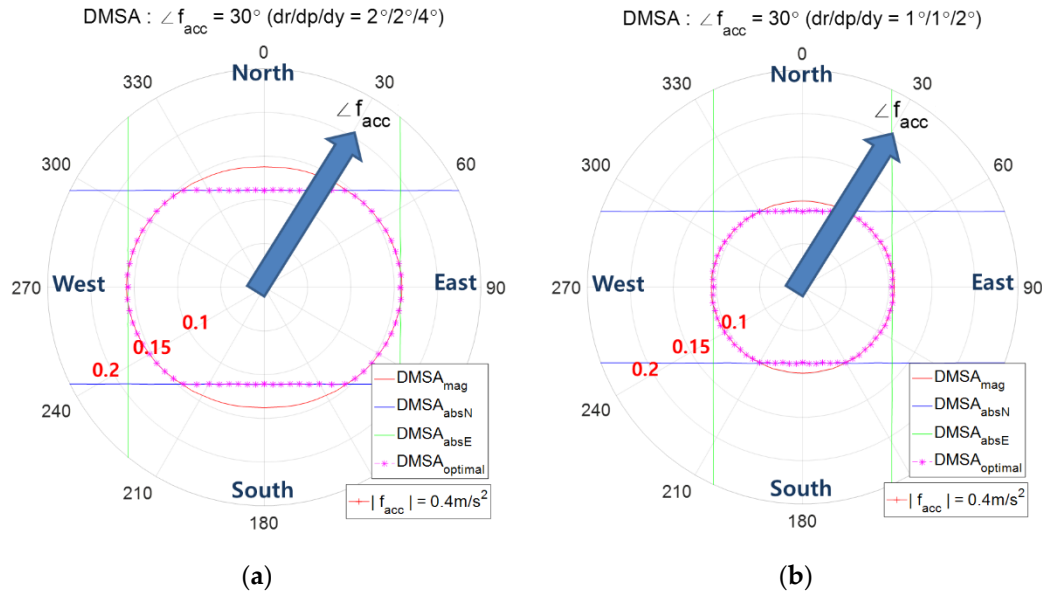


Figure 15. Combined Contour of DMSA with respect to the AHRS attitude accuracy.

Figure 16a,b show the case of $\angle f_{acc} = 30^\circ$ and $\angle f_{acc} = 120^\circ$, respectively, with $|f_{acc}| = 0.2, 0.4, 0.6 \text{ m/s}^2$. The decision variable z_{absN} is used for $\angle f_{acc} = 30^\circ$ and z_{absE} is used for $\angle f_{acc} = 120^\circ$. It is observed that as $|f_{acc}|$ increases, the range of angles using z_{absN} (or z_{absE}) becomes larger.

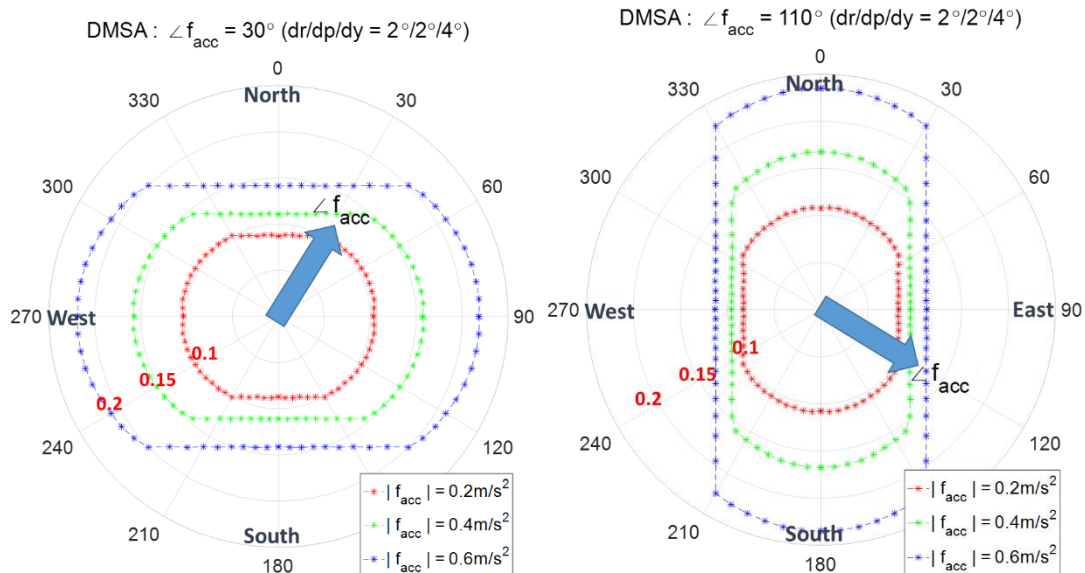


Figure 16. Combined contour of DMSA with respect to the magnitude of f_{acc} .

Figure 17 shows the case of $\angle f_{acc} = 45^\circ$ and the decision variables z_{mag} , z_{absN} and z_{absE} are all necessary to obtain the optimal combined contour.

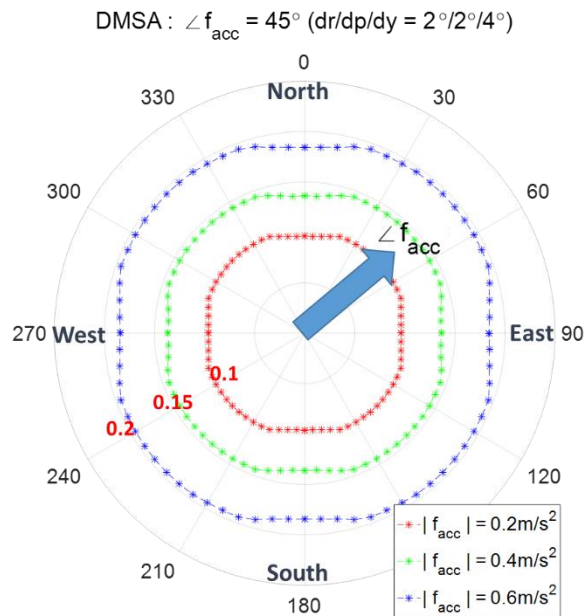


Figure 17. Combined contour of DMSA with respect to the magnitude of $\angle f_{acc} = 45^\circ$.

6. Conclusions

In this study, a direct GPS spoofing detection method is proposed, with AHRS and accelerometers via the difference of the acceleration estimated from GPS receiver and the acceleration measured from IMU. From the acceleration error expressed in the navigation frame, two decision variables are defined for spoofing detection. One decision variable z_{mag} , which may be commonly used, is defined as the magnitude of the horizontal acceleration error. The other decision variable z_{absN} (or z_{absE}) is defined as the magnitude of the north (or east) component of the acceleration error.

The spoofing detection performance can be evaluated using the detection probability, which can be calculated from the probability density function of both decision variables. The decision variable z_{absN} shows higher detection probability than z_{mag} in the condition that both moving acceleration and spoofing acceleration are heading within roughly 25° from the north or south. Similarly, the decision variable z_{absE} shows higher detection probability than z_{mag} in the condition that both moving acceleration and spoofing acceleration are heading within roughly 25° from the east or west.

When detectable minimum spoofing acceleration (DMSA) is used, the decision variable z_{absN} (or z_{absE}) shows smaller DMSA than z_{mag} in the condition that both moving acceleration and spoofing acceleration head are within roughly 25° from the north-south direction (or east-west direction).

The spoofing acceleration can happen to be any direction. Thus, given a pre-defined false alarm probability, the best algorithm to detect GPS spoofing is that the three decision variables z_{mag} , z_{absN} , and z_{absE} are calculated and compared with the corresponding threshold, and declare the existence of the GPS spoofing if any of the three decision variables exceed the corresponding threshold.

The proposed GPS spoofing detection method in this paper depends on the acceleration error. If a ground vehicle runs across road irregularities such as potholes, bumps, and rubble, etc., then accelerometers may show large changes and deteriorate the GPS spoofing detection performance. Therefore, the flying or driving environment may have an effect on the GPS detection performance.

Author Contributions: Conceptualization, D.-S.S.; Formal analysis, D.-S.S.; Software, K.-C.K.; Supervision, D.-S.S.; Writing—original draft, K.-C.K.; Writing—review & editing, D.-S.S.; Derivation of Shim probability density function, D.-S.S. All authors have read and agreed to the published version of the manuscript.

Funding: This research received no external funding.

Conflicts of Interest: The authors declare no conflict of interest.

References

1. Kaplan, E.D. *Understanding GPS, Principles and Applications*, 2nd ed.; Artech House: Norwood, MA, USA, 2006; pp. 123–132.
2. Tsui, J.B.-Y. *Fundamentals of Global Positioning System Receivers: A Software Approach*, 2nd ed.; Wiley: Hoboken, NJ, USA, 2005; pp. 73–78.
3. Volpe, J.A. Vulnerability Assessment of the Transportation Infrastructure Relying On the Global Positioning System. *J. Naviga.* **2003**, *56*, 185–193.
4. Warner, J.; Johnston, R. A Simple Demonstration That the Global Positioning System (GPS) is Vulnerable to Spoofing. *J. Secur. Admin.* **2002**, *25*, 19–28.
5. Humphreys, T.E.; Ledvina, B.M.; Psiaki, M.L.; O Hanlon, B.W.; Kintner, P.M., Jr. Assessing the Spoofng Threat—Development of a Portable GPS Civilian Spoofe. In Proceedings of the 2008 ION GNSS Conference, Savanna, GA, USA, 16–19 September 2008; pp. 1–12.
6. Tippenhauer, N.O.; Pöpper, C.; Rasmussen, K.B.; Capkun, S. On the Requirements for Successful GPS Spoofing Attacks. In Proceedings of the 18th ACM Conference on Computer and Communications Security, CCS 2011, Chicago, IL, USA, 17–21 October 2011; pp. 1–11.
7. Cavalieri, A.B.; Motella, M.P.; Fantino, M. Detection of Spoofed GPS Signals at Code and Carrier Tracking Level. In Proceedings of the 5th ESA Workshop on Satellite Navigation Technologies and European Workshop on GNSS Signals and Signal Processing (NAVITEC), Noordwijk, The Netherlands, 8–10 December 2010; pp. 1–6.
8. Wen, H.; Huang, P.Y.-R.; Dyer, J.; Archinal, A.; Fagan, J. Countermeasures for GPS Signal Spoofing. In Proceedings of the 18th International Technical Meeting of the Satellite Division of The Institute of Navigation (ION GNSS 2005), Long Beach, CA, USA, 13–16 September 2005.
9. Dehghanian, V.; Nielsen, J. GNSS Spoofing Detection Based on a Sequence of RSS Measurements. *ION GPS GNSS* **2013**, *26*, 2931–2935.
10. Borio, D. PANova Tests and their Application to GNSS Spoofing Detection. *IEEE Trans. Aerosp. Electron. Syst.* **2013**, *49*, 381–394. [[CrossRef](#)]
11. Wang, F.; Li, H.; Lu, M. GNSS Spoofing Detection and Mitigation Based on Maximum Likelihood Estimation. *Sensors* **2017**, *17*, 1532. [[CrossRef](#)] [[PubMed](#)]
12. Jafarnia-Jahromi, A.; Broumandan, A.; Nielsen, J.; Lachapelle, G. GPS Vulnerability to Spoofing Threats and a Review of Anti-spoofing Techniques. *Int. J. Navig. Obs.* **2012**, *2012*, 127072.
13. Wesson, K.D.; Shepard, D.P.; Humphreys, T.E. Straight talk on anti-spoofing. *GPS World* **2012**, *23*, 32–39.
14. Konovaltsev, A.; Cuntz, M.; Haettich, C.; Meurer, M. Autonomous Spoofing Detection and Mitigation in a GNSS Receiver with an Adaptive Antenna Array. *ION GPS GNSS* **2013**, *26*, 2937–2948.
15. Swaszek, P.F.; Pratz, S.A.; Arocho, B.N.; Seals, K.C.; Hartnett, R.J. GNSS Spoof Detection Using Shipboard IMU Measurements. In Proceedings of the 27th International Technical Meeting of the Satellite Division of the Institute of Navigation (ION GNSS+ 2014), Tampa, FL, USA, 8–12 September 2014; pp. 745–758.
16. Khanafseh, S.; Roshan, N.; Langel, S.; Chan, F.-C.; Joerger, M.; Pervan, B. GPS Spoofing Detection using RAIM with INS Coupling. In Proceedings of the PLANS 2014, 2014 IEEE/ION, Monterey, CA, USA, 5–8 May 2014; pp. 1232–1239.
17. Tanil, C.; Khanafseh, S.; Joerger, M.; Pervan, B. An INS monitor to detect GNSS spoofers capable of tracking vehicle position. *IEEE Trans. Aerosp. Electron. Syst.* **2017**, *54*, 131–143. [[CrossRef](#)]
18. Lee, J.-H.; Kwon, K.-C.; An, D.-S.; Shim, D.-S. GPS Spoofing Detection using Accelerometers and Performance Analysis with Probability of Detection. *Int. J. Control Autom. Syst.* **2015**, *13*, 951–959. [[CrossRef](#)]
19. Bekkeng, J.K. Calibration of a Novel MEMS Inertial Reference Unit. *IEEE Trans. Instrum. Meas.* **2009**, *58*, 1967–1974. [[CrossRef](#)]
20. Gao, W.; Zhang, Y.; Wang, J. Research on Initial Alignment and Self-Calibration of Rotary Strapdown Inertial Navigation Systems. *Sensors* **2015**, *15*, 3154–3171. [[CrossRef](#)] [[PubMed](#)]
21. Grewal, M.S.; Andrews, A.P. *Kalman Filtering Theory and Practice*; Prentice Hall: Englewood Cliffs, NJ, USA, 1993; pp. 108–118.
22. Han, S.; Wang, J. A novel method to integrate IMU and magnetometers in attitude and heading reference systems. *J. Navig.* **2011**, *64*, 727–738. [[CrossRef](#)]

23. Khedr, M.; El-Sheimy, N. A Smartphone Step Counter Using IMU and Magnetometer for Navigation and Health Monitoring Applications. *Sensors* **2017**, *17*, 2573. [[CrossRef](#)]
24. Hellmers, H.; Kasmi, Z.; Norrdine, A.; Eichhorn, A. Accurate 3D Positioning for a Mobile Platform in Non-Line-of-Sight Scenarios Based on IMU/Magnetometer Sensor Fusion. *Sensors* **2018**, *18*, 126. [[CrossRef](#)] [[PubMed](#)]
25. Patonis, P.; Patias, P.; Tziavos, I.N.; Rossikopoulos, D.; Margaritis, K.G. A Fusion Method for Combining Low-Cost IMU/Magnetometer Outputs for Use in Applications on Mobile Devices. *Sensors* **2018**, *18*, 2616. [[CrossRef](#)]
26. Hoyt, R.S. Probability functions for the modulus and angle of the normal complex variate. *Bell Syst. Tech. J.* **1947**, *26*, 318–359. [[CrossRef](#)]
27. Youssef, N.; Wang, C.-X.; Pätzold, M. A Study On The Second Order Statistics Of Nakagami Hoyt Mobile Fading Channels. *IEEE Trans. Veh. Technol.* **2005**, *54*, 1259–1265. [[CrossRef](#)]
28. Tsagris, M.; Beneki, C.; Hassani, H. On the Folded Normal Distribution. *Mathematics* **2014**, *2*, 12–28. [[CrossRef](#)]



© 2020 by the authors. Licensee MDPI, Basel, Switzerland. This article is an open access article distributed under the terms and conditions of the Creative Commons Attribution (CC BY) license (<http://creativecommons.org/licenses/by/4.0/>).